

Approximate analog computing with metatronic circuits

Mario Miscuglio ^{1✉}, Yaliang Gui¹, Xiaoxuan Ma¹, Zhizhen Ma¹, Shuai Sun¹, Tarek El Ghazawi¹, Tatsuo Itoh², Andrea Alù ³ & Volker J. Sorger ^{1✉}

Analog photonic solutions offer unique opportunities to address complex computational tasks with unprecedented performance in terms of energy dissipation and speeds, overcoming current limitations of modern computing architectures based on electron flows and digital approaches. The lack of modularization and lumped element reconfigurability in photonics has prevented the transition to an all-optical analog computing platform. Here, we explore, using numerical simulation, a nanophotonic platform based on epsilon-near-zero materials capable of solving in the analog domain partial differential equations (PDE). Wavelength stretching in zero-index media enables highly nonlocal interactions within the board based on the conduction of electric displacement, which can be monitored to extract the solution of a broad class of PDE problems. By exploiting the experimentally achieved control of deposition technique through process parameters, used in our simulations, we demonstrate the possibility of implementing the proposed nano-optic processor using CMOS-compatible indium-tin-oxide, whose optical properties can be tuned by carrier injection to obtain programmability at high speeds and low energy requirements. Our nano-optical analog processor can be integrated at chip-scale, processing arbitrary inputs at the speed of light.

¹Department of Electrical and Computer Engineering, The George Washington University, Washington DC, USA. ²Electrical Engineering Department, University of California, Los Angeles, CA, USA. ³Department of Electrical Engineering, Grove School of Engineering, City College of New York, New York, NY, USA. ✉email: mmiscuglio@gwu.edu; sorger@gwu.edu

Current computing tasks are characterized by an elevated level of complexity and therefore require high computational cost. A major criticality of today's digital computing is related to the required computational power, which does not scale well with the problem complexity. For this reason, developing innovative analog accelerators, which could take the load off from traditional computers by solving specific complex processes, holds the promise to significantly reduce energy consumption and can lead to the development of next-generation heterogeneous computing systems. Analog computers are not a recent invention and are, in fact, well-rooted in human history prior to this digital age, being applied to a vast variety of fields¹. While digital processing became dominant in the preceding 50 years, recently, several research groups explore innovative solutions to address growing compute-limitation to business-as-usual. This trend favored the advancement of several non-Von Neumann hardware architectures, which aim to homomorphically map specific algorithms directly into hardware. Analog memory^{2,3}, neuromorphic photonics for deep learning applications⁴⁻⁷, optical co-processors for high-speed convolutions⁸, integral equation solvers⁹, and quantum analog computers¹⁰ are only some examples of currently explored analog architectures, which can tackle complex tasks more efficiently than a conventional digital processor.

One of the mathematical tasks that can exploit these paradigms and may greatly benefit from using analog co-processors, and the object of this study, is solving partial differential equations (PDEs). In fact, numerous scientific and engineering problems require the solution of PDEs¹¹, such as problems in thermodynamics¹², aircraft design¹³, and others in electrical and mechanical engineering field¹⁴. For solving multidimensional PDEs, current processors require a large number of (iterative) operations, which are computationally intensive, and, based on the complexity, necessitate considerable amount of memory and power¹⁵. Analog computers capable of solving PDEs have been implemented since the 1950s¹¹; primarily using networks or grids of resistive or reactive elements to model the spatial distribution of physical quantities such as voltage, current, and power (in electric distribution networks), electrical potential in space, stress in solid materials, temperature (in heat diffusion problems), pressure, fluid flow rate, and wave amplitude. However, the complexities of an effective integration of a high-speed-programmable and concurrently energy-efficient static-like analog mesh significantly reduced the advancement of this technology.

Novel compute systems are often enabled by new hardware platforms, such as metatronics, which was introduced by Engheta a decade ago as the branch of optics that focuses on the control of light at the nanoscale through metamaterial-inspired optical nanocircuitry. Thus, metatronics offers an avenue for designing dense circuits and analog compute paradigms. Despite finding diverse applications, such as ultra-thin sub-wavelength filters for optical signal^{16,17}, circuit for performing mathematical operations^{9,18}, and for modeling Hamiltonian of quantum system^{19,20}, its application as an alternative integrated platform for implementing a compact analog reprogrammable processor is still outstanding. The applicability of the metatronic concepts has, so far, been limited by four main factors: (a) the lack of availability of materials required to realize its individual circuit elements, (b) the absence of controlled processes for straightforward fabrication, (c) lack of reprogrammability, "write", and (d) difficulties in accessing the results, "read".

Here, we introduce a nanoscopic programmable analog processor based on a metatronic nanocircuit board aiming to map a finite difference PDE onto a mesh similar to a network of resistors, but in an integrable and ultra-compact fashion using nano-optics. We design and show through numerical simulation, an ultra-compact nano-optic circuit design based on air groove

meshes, engraved into indium tin oxide (ITO) substrate, operating at its epsilon-near-zero (ENZ) wavelength. We show that such a metatronic circuit, mimicking an electrical lumped circuit, demonstrates the ability to solve PDEs using finite difference. We demonstrate, assisted by experimentally derived optical characterization and control of deposition techniques, that ITO nanoelements exhibiting resistive, inductive, and capacitive behavior, sputtered using different sputtering conditions²¹, can be embedded within the air grooves. Electrostatically fine-tuning their optical properties at high speed²² through carrier accumulation/depletion enables approximate solutions to a variety of PDEs, including Laplace equation, Poisson equation, diffusion equation, and wave equation. Interestingly, the power consumption to obtain an approximate discretized solution is effortlessly computed within the transit time of the electromagnetic wave propagates in the chip, once the chip is set to a particular boundary condition. In this view, we ultimately envision the implementation of an all-optical readout paradigm based on a near-field optical microscopy measurement, providing information of the local dielectric displacement, at given points of the nano-optics circuit, thus allowing to extract the results of the computation in a discretized manner. Such wavelength-scale analog compute nodes can offer a variety of functionality in compact and efficient signal processing, computing, or artificial intelligence.

Results and discussion

Metatronic circuit as a PDE finite difference solver. Before beginning the description of the nano-optic accelerator, we ought to describe a metatronic mesh and how it compares to a finite difference and lumped resistive meshes. (Fig. 1a) We start by considering the steady-state homogeneous Laplace's differential equation, where $f(x, y)$ is the distribution of the physical entity (i.e., PDE solution) of the two-dimensional (2D) domain (i.e., mesh). As a relevant example, we select the homogeneous heat equation, because it is widely employed in a variety of mathematical and engineering problems, ranging from machine learning in graph Laplacian methods²³ to image analysis^{24,25}. Then,

$$\nabla^2 f = 0, \quad (1)$$

where the field f in the case of the heat equation denotes the temperature distribution, and can be written in the Cartesian 2D space via

$$\frac{\partial^2 f}{\partial x^2} + \frac{\partial^2 f}{\partial y^2} = 0 \quad (2)$$

The same equation may eventually represent a steady-state distribution of temperature, as well as stress distributions, potential, and flows. (Fig. 1b.i) The finite difference method allows current processors to iteratively solve differential equations, such as Eq. 2, by approximating them via a difference equation, in which finite differences approximate the derivatives. Considering equidistant points in the domain (and constant point function ϵ_i), Eq. 2 can be approximated via the finite difference relaxation method (Fig. 1b), at the point O of a mesh, as¹¹:

$$\nabla^2 f = \frac{1}{h^2} [f(P_1) + f(P_2) + f(P_3) + f(P_4) - 4f(P_1)] \quad (3)$$

The finite difference equation can be straightforwardly compared to the application of Kirchhoff's law to the currents $f(P_i)$ netting at the junction O of a lumped circuit mesh (Fig. 1b), where resistances are opportunely scaled ($R = h^2$). Ohm's law, in fact, shows a linear relationship between voltage and current, whilst Kirchhoff's law states that the input and output of current into a node will always be equal.

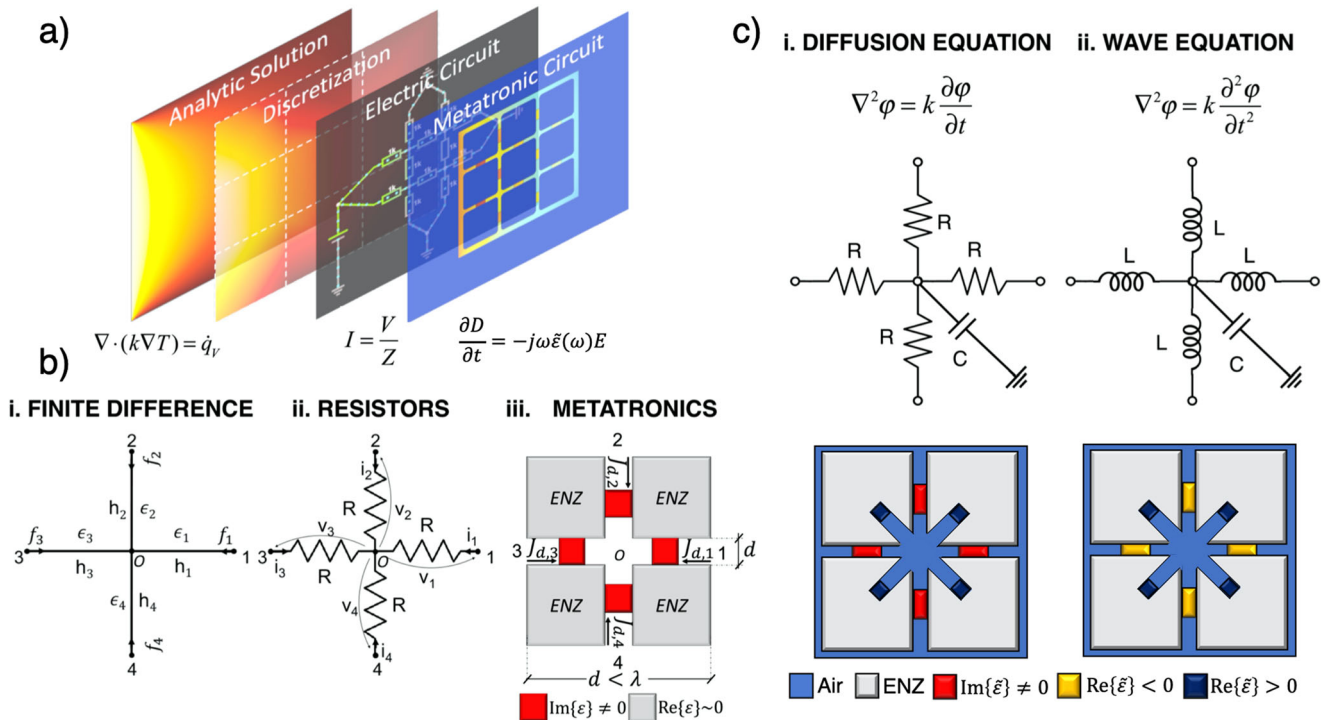


Fig. 1 Solving partial differential equation with metatronics. **a** Sketch of the mapping from a generic partial differential equation to a metatronic circuit, passing through the discretization of finite differences and related Kirchhoff’s lumped-element equivalent circuit. The schematic shows the solutions of a steady-state heat transfer problem with Dirichlet’s boundary conditions obtained analytically, and in a discretized fashion with a defined mesh density. The discretized problem is successively converted into a resistive circuit problem which can be ultimately converted into a metatronic circuit in which the nano-optical elements are coupled and the light traveling through it is not affected by any phase variation or transit time. **b** Node equivalence between finite difference (i), resistive mesh (ii), and metatronics using epsilon-near-zero (ENZ) board and air trenches (iii). A finite difference method (i) applied to a heat transfer problem (Laplace equation) is mapped to a purely resistive network and a nano-optic circuit in which the constant point function, ϵ_i , are replaced by resistors in the electrical (ii) and lossy dielectric in the nano-optic circuit (iii), respectively. The finite differences of the function f , netting at point O , are represented as electrical currents in the electrical circuit (ii) and displacement currents, $J_{D,i}$ (iii) **c** Generality of the approach: introducing different nanoelements, either resistive (red block, $\text{Im}\{\tilde{\epsilon}\} \neq 0$), capacitive (dark blue, $\text{Re}\{\tilde{\epsilon}\} > 0$) or inductive (yellow, $\text{Re}\{\tilde{\epsilon}\} < 0$), lead to the implementation of diverse time variant second-order PDE, such as Diffusion equation (i) and Wave equation (ii). In these configurations, for avoiding continuity of the current, the nano-capacitor is placed in a “shunt” configuration with respect to the node. Here, for preserving the symmetry of the node, the current splits into 4 different channels. Alternatively, a nanocapacitor in shunt configuration can be placed at the node O , extruding the ENZ board, and related air trench, in the third dimension.

According to these equivalences, as previously proposed^{26,27}, approximate experimental solutions of Laplace’s and Poisson’s boundary value problems can be obtained using networks of electrical resistances with a rather low tolerance²⁶. The measurement of voltage values at grid points provides the equivalent discrete solution for given resistor values. However, when the parameters of the circuits are programmed at a given rate (i.e., write speed) and its inputs initiated, then an electric mesh might be affected by resistive-capacitive (RC) time delay. Moreover, at high speeds the time at which the signal changes become comparable to the propagation time in the circuit, which therefore makes it into a distributed network. Under these conditions, the circuit would lose the ability to map a finite difference mesh-grid that is able to solve PDEs. For this reason, a processor capable of solving PDEs using nano-optics circuitry is highly desirable. Here, we exploit the fact that sub-wavelength nanoparticles (NPs) in the optical domain can be treated as lumped circuit elements, whose impedance is defined in terms of the induced displacement current j_D , in response to the local electric field E . According to Maxwell’s equations, $\tilde{\epsilon}$, the complex material permittivity, relates these two quantities through

$$J_D = \frac{\partial D}{\partial t} = -j\tilde{\epsilon}\omega E(\omega), \tag{4}$$

which, for element size considerably smaller than the optical wavelength ($d \ll \lambda$)²⁸, represents an equivalent Ohm’s law in the

optical domain, enabling the mapping of the resistive circuit. Nevertheless, arranging different NPs with absolute control on permittivity and position is far from easy^{29,30}, and as the size of the circuit grows it is challenging to make sure that the flux of displacement current is funneled to ensure the required circuit connections without phase delays. For these reasons, ENZ substrates are ideal for the implementation of nanocircuit boards, as they enable light to travel through the grooves just like electric currents in copper wiring³¹ (Fig. 1b.iii). Resistors, capacitors, and inductors can be implemented within the air grooves by tailoring the local permittivity values. To map Eq. 3 in the metatronics paradigm, the resistors are modeled as dissipative dielectrics. Due to the confinement of displacement current in the air grooves³², as in an ideal ENZ substrate there is no displacement current leakage in the background, the circuit elements are locally coupled, implying that the Norton/Thévenin equivalents are admissible. In other words, local variations in the network generate global effects. Therefore, for a limited functional bandwidth over which the material of the board is ENZ (proportional to the full-width at half-maximum of the ENZ resonance peak), Kirchhoff’s law is satisfied in the mesh, resulting in identical results with respect to a resistive network, reported in Eq. 3.

A node of a metatronic mesh, equivalent to a resistive one, is represented in Fig. 1b. This approach is not limited to resistive networks and consequently to Laplace homogeneous equations.

Indeed, by using plasmonic NPs (negative permittivity) to construct nanoinductors and dielectric nanoelements (positive permittivity) for nanocapacitors, it is possible to map other time-dependent PDEs applied to a 2D mesh, such as diffusion or wave equation (Fig. 1c).

Programmability of the nano-optic elements. In order to prove the ability to reprogram the circuit and control its electromagnetic response³³, in this section, we aim to demonstrate that different lumped-element functionalities can be achieved in ITO films by modulating the free carriers of the ITO nanoelements via electrostatic doping.

In detail, an electrical voltage bias can be applied across a capacitor, whose plate is the ITO film, and according to the bias polarity an accumulation/depletion layer is formed at the ITO–oxide interface, increasing/decreasing locally the ITO’s carrier density ($1 \times 10^{19} - 1 \times 10^{21} \text{ cm}^{-3}$)^{34–36}, which ultimately alters its complex optical properties.

For doing so, we use a straightforward, yet effective, demonstration of a programmable nano-optic circuit based on ITO in which a meta-ring is engraved in an ITO substrate, defining an air loop (Fig. 2a). The optical response of the system is obtained by performing a full-wave electromagnetic simulation of an ITO layer. An electric field is driven by a dipole (quantum dot, QD) placed within the channel, forming a directional flow of the displacement current when the ITO layer is in the ENZ range. By way of an example, in the simulation, the QD is considered as point source, neglecting far-field to near-field coupling. In this case, we optimized the air trench of width 0.1λ to form a closed loop with an average total length of $2\pi r = 2440 \text{ nm}$ which is twice the wavelength, and it is sufficiently small for supporting TE_{10} -like mode excited by a dipole and concurrently does not experience phase variation within the trenches. In Supplementary Fig. 2a, b we provide the eigenmode analysis as function of the width and height of the air trenches. For this exemplary-selected condition, the characteristic length scale of the nano-optic chip (D) is considerably smaller than the effective wavelength, therefore guaranteeing quasi-static approximation ($D < \lambda_{\text{eff}}$, $D < \lambda$, $\pi D \sim \lambda_{\text{eff}}$).

It is worth noticing that suitable QDs for these wavelengths are scarce³⁷ and usually comparable in size with the trenches. For this reason, the trenches can be modified to host the source, while preserving excitation, coupling, and mode propagation (Supplementary Fig. 11).

The dispersion of the ITO layer can be electrostatically tuned by varying the carrier concentration (Fig. 2b), thus changing the behavior at a given operating frequency. We evaluate the spectral response of the meta-ring, by averaging the field displacement within the air groove for three different carrier concentrations: (i) depletion (ii) ENZ, and (iii) accumulation (Fig. 2c, d).

It is worth observing that for different carrier concentrations we obtain a similar response, energy shifted in the same fashion as at the ENZ resonance, indicating a moderately robust response. Additionally, the spectral response is archetypal of a low-pass frequency filter (long-pass wavelength), i.e., integrator-type, since we are considering a voltage drop on a capacitor (dielectric air loop) hosted by a resistive circuit board (lossy ENZ) of the equivalent lumped circuit. We then fix the excitation wavelength of the film at the ENZ crossing point for the as-deposited case ($1 \times 10^{21} \text{ cm}^{-3}$) and take a snapshot of the simulation result of the distribution of the field displacement and current density in the middle plane. In the first scenario (i) when ITO is depleted of its carriers, the material turns dielectric (capacitance, ENZ red-shift), providing relatively low losses ($\epsilon'(\lambda_{\text{ENZ}}) > 0$, $\epsilon''(\lambda_{\text{ENZ}}) \sim 0$). As a direct consequence, the displacement field in the board hosting the channels becomes

non-negligible; (ii) on the other hand, when the excitation matches the ENZ wavelength ($\epsilon'(\lambda_{\text{ENZ}}) = 0$, $\epsilon''(\lambda_{\text{ENZ}}) > 0$), the air loop behaves as D-dot, in which the displacement current circulates in the loop with relatively low losses; (iii) however, when carriers are accumulated, ITO exhibits a predominantly metallic behavior (inductance, ENZ blue-shift) characterized by higher ohmic losses ($\epsilon'(\lambda_{\text{ENZ}}) < 0$, $\epsilon''(\lambda_{\text{ENZ}}) \gg 0$). Equivalent circuit which maps the nano-optic response are displayed as insets (Fig. 2d).

Meta-resonator. For demonstrating the generality of this approach, it is possible to introduce reprogrammable nanoelements for implementing different chip functionality. At ENZ wavelength, the specific response of lumped elements (R, L, C) can be achieved by partially filling the air grooves with ITO nanoelements electrostatically modulated with specific voltage polarity. For illustrative purposes, we design the equivalent of an electronic resonator.

Following the characterization of the meta-ring, next we introduce nano-optic elements within the air trench, thus adding resonator tunability to the system towards adaptation functionality of the nanoscale “filter” (Fig. 3a). The nanoelements are physically realized with the same basic material as the ENZ circuit board, namely ITO, however, bear a different carrier density to exhibit an RL or RC element. Note, this is realized either statically such as via changing the material process conditions during the ITO sputter recipe, and/or actively (i.e., electrostatic tuning) towards delivering element-wise independent tunability of sub-wavelength small (i.e., lumped) elements (Fig. 3b). As a demonstration, here we consider one element to be injected with carriers (L) and the other one depleted (C), resulting into an LCR-like behavior at the ENZ wavelength. Note, since ITO’s index tunability originates from free carrier modulation and the carrier densities are rather high (even in the depleted case, i.e., depleted here refers to a reduced carrier concentration, not void-of-carriers), an EM wave impeding ITO will always experience a non-zero imaginary optical index, this adding loss, which electrically resembles a resistance R. Thus, a pure C or pure L element is not simply possible in ITO unless gain or loss-compensation methods are used. Our model nanocircuit considered here acts as a nano-optic resonator storing energy oscillating at the circuit resonant frequency calibrated to be at ENZ (Supplementary Movie 2).

In an electrical RLC circuit, the voltage drop on a capacitance and inductance are represented by the following rational functions:

$$V_C(\omega) = \frac{1}{-\omega^2 LC + 1} V_{\text{in}}, \quad V_L(\omega) = \frac{\omega^2 LC}{\omega^2 LC - 1} V_{\text{in}} \quad (5)$$

The function $V_C(\omega)$ is characterized by two poles in $\omega = 1/\sqrt{LC}$, while $V_L(\omega)$ has two zeros at 0 frequency and 2 poles in $\omega = 1/\sqrt{LC}$. Besides the correct mapping of the optical circuit at ENZ, the anticipated low-pass (LP)/high-pass (HP) frequency response of the electrical circuit is not perfectly mapped by the dielectric displacement in the ITO nano-optics circuit for each wavelength (Fig. 3d). This is primarily due to three factors:

(i) ITO nanoelements are affected by a strong dispersion are functions of the wavelength unlike the electrical counterpart. More in detail, the optical impedances can be written as:

$$Z_C(\omega) = (-i\omega C(\omega))^{-1} \text{ with } C = \epsilon'_c(\omega)\epsilon_0 t/l \text{ being } \tilde{\epsilon}_c(\omega) \sim \epsilon'_c(\omega) \\ Z_L(\omega) = i\omega L(\omega) \text{ with } L = -l/(\omega^2 \tilde{\epsilon}_L(\omega)\epsilon_0 t) \quad (6)$$

considering l and t , length and thickness of the nano-optic element, respectively, and ω the optical angular frequency. It can be noticed that the dielectric displacement (and consequently the

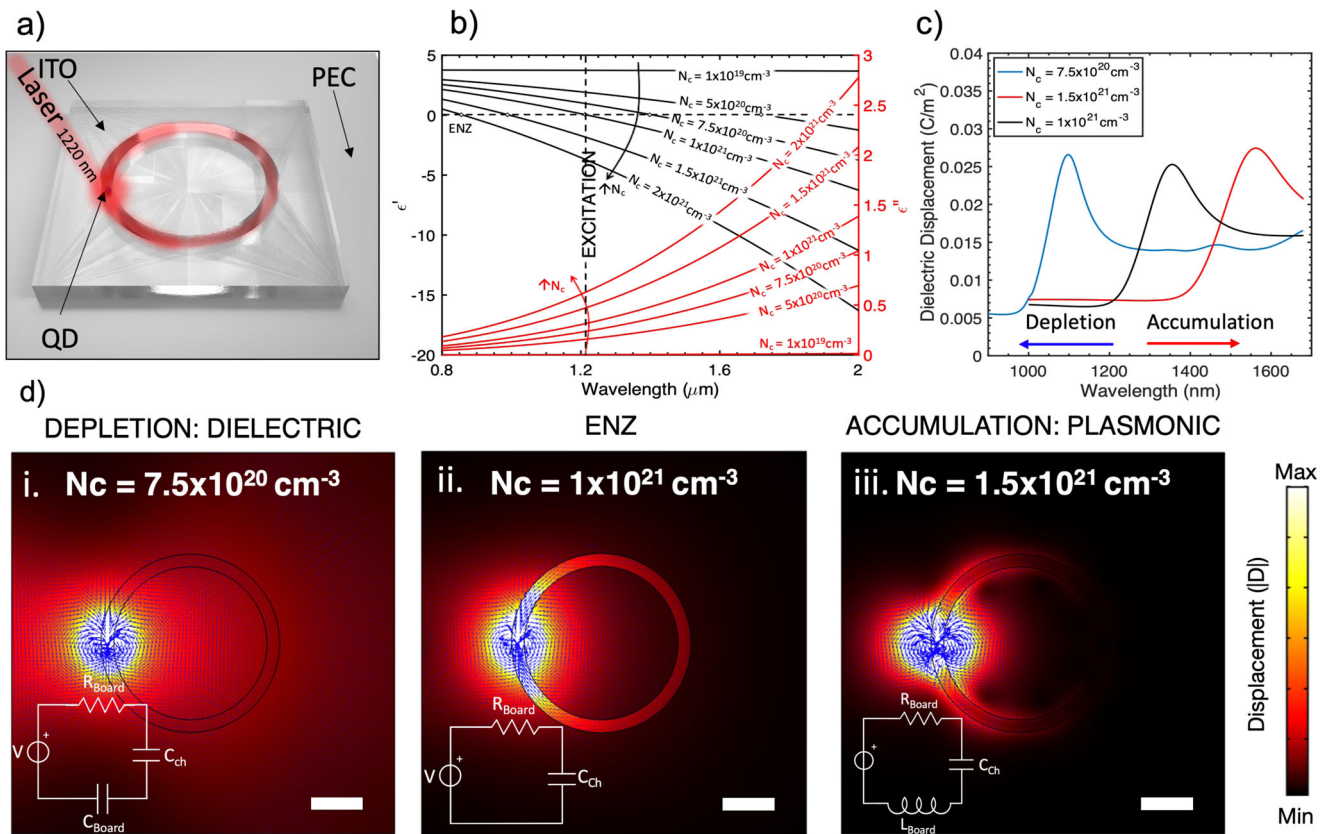


Fig. 2 Epsilon-near-zero tunable meta-ring. **a** Schematic representation of a meta-ring engraved in an indium tin oxide (ITO) layer. The dielectric displacement field within the trench is generated by a dipole, i.e., emitting nanoparticle at 1220 nm, which is in resonance with the epsilon-near-zero (ENZ) crossing point of the ITO layer. The boundary of the ITO board are considered to be perfect electric conductor (PEC). **b** For simulating the spectral response of the meta-ring we consider experimentally derived optical properties using spectroscopic ellipsometry. When the ITO carrier concentration is unaltered (as-deposition), the ITO film displays a carrier concentration of $1 \times 10^{21} \text{ cm}^{-3}$, mobility $38 \text{ cm}^2 \text{ V}^{-1} \text{ s}^{-1}$ and scattering rate $\tau_{sc} = 7 \text{ fs}$, which translates to an ENZ wavelength of $1.2 \mu\text{m}$. The model for the “active” dispersion is obtained by fitting experimental ellipsometry data using Drude’s model (Supplementary Fig. 6). The active tuning is envisioned to be obtained by means of carrier injection in a capacitor configuration. The horizontal and vertical dashed lines indicate the ENZ crossing point and the ENZ wavelength of the intrinsic device. **c** Simulated average dielectric displacement within the air groove for different carrier concentrations: depletion ($7.5 \times 10^{20} \text{ cm}^{-3}$), intrinsic ($1.0 \times 10^{21} \text{ cm}^{-3}$), and accumulation ($1.5 \times 10^{21} \text{ cm}^{-3}$). **d** Numerically derived displacement field and equivalent electrical circuit for various carrier concentration of the ITO layer. Blue arrows represent the displacement current: (i) for low carrier concentration ITO board behaves as dielectric with low losses; (ii) for a higher concentration ($1 \times 10^{21} \text{ cm}^{-3}$) the displacement field is within the air trench; and (iii) for furtherly higher carrier concentration, the film is metallic with high losses. Scale bar 200 nm. Time domain response of the meta-ring shown in Supplementary Note 1 and Supplementary Movie 1 highlights ring behavior for the different regimes. Color bar represents the normalized dielectric displacement.

electric field) within the capacitance is in counter phase with respect to the phase in the inductance (Fig. 3c), as expected. (ii) The static-like behavior of the metatronic board is guaranteed only at ENZ; (iii) optical losses in the circuit boards.

As shown in Supplementary Movie 2, the energy bounces between a nano-optic inductance and capacitance, thus proving that nano-optic circuits, entirely based on ITO, can be used as programmable oscillators or filters for tuning transmitters and receivers in the telecommunication bandwidth. When electrostatically tuned, the permittivity of the ITO nanoelements can map different problems. Although, when the carriers are electrostatically modulated, Kramers–Kronig (KK) relation dictates that exclusive change of the real part (or imaginary part) of the complex index is not achievable. As the real part decreases with modulation (Δn), the imaginary part increases ($\Delta \kappa$), affecting the performance of the nano-optic circuit, as the equivalent of capacitances or inductances are unwantedly added. Phase change materials that exhibit large Δn with relatively broad transparencies³⁸ can be considered for future implementation, especially in regards of their nonvolatile

retention of the information, which enables near-zero static power consumption (i.e., no voltage needs to be applied to retain the programmed state). It is also worth mentioning that the ITO region in which the carriers are accumulated is within several nanometers and the $1/e^2$ decay-length is only about 10 nm ^{36,39,40}, extended in the simulation to the entire nanoelement. However, the desired extinction ratio can be also adjusted by the applied voltage at the expense of (static) power consumption for a selected design. However, considering the tight confinement within the trenches and slow-light effect, thanks to a high Δn_{eff} , it is possible to achieve high modulation even in relatively short devices²².

Therefore, in principle, the nano-optic elements in the proposed ITO-based nonphotonic chip should be deposited using specific process parameters to achieve the desired permittivity according to chosen functionality (capacitance, inductance, and resistance), while fine-tuning can be achieved using carrier modulation. In terms of PDE mapping, this means that a circuit can solve a class of PDE whose coefficient can be modified by tuning the optical properties of its nanoelement.

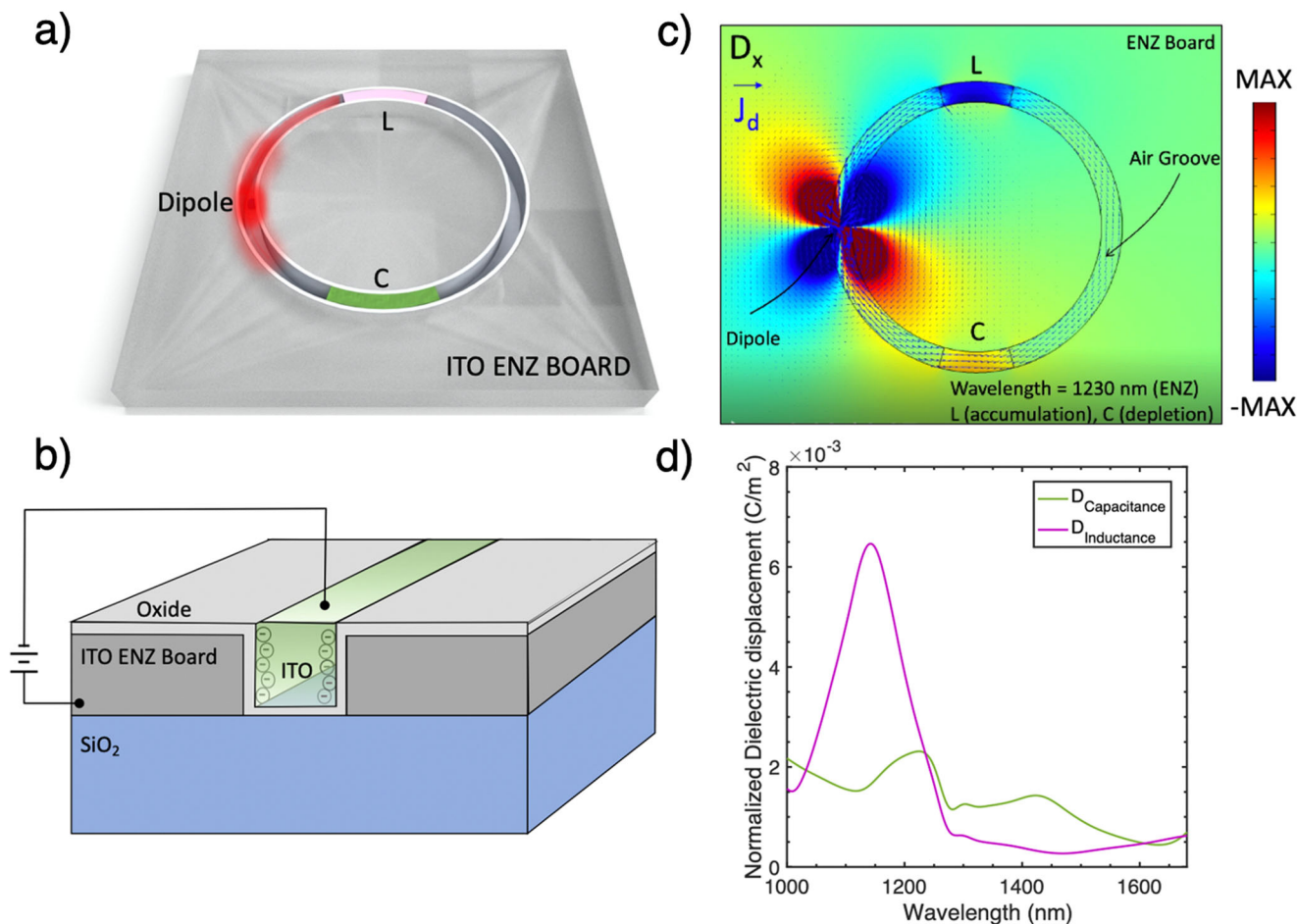


Fig. 3 Meta-resonator. **a** Schematic representation of the nano-optic circuit mimicking an RLC optical lumped circuit at epsilon-near-zero (ENZ) and **b** related bias mechanism for modulating the carrier density of an indium tin oxide (ITO) nanoelement, in order to reprogram the optical circuit to exhibit a particular frequency response, thus acting as a programmable filter. The functionality of each nanoelement is obtained through electrostatic doping in a capacitor configuration. Carrier depletion ($7.5 \times 10^{20} \text{ cm}^{-3}$) prompts a capacitor behavior, while carrier accumulation ($1.25 \times 10^{21} \text{ cm}^{-3}$) induces an inductance behavior. **c** Simulation results for the x-component of the displacement field induced by a dipole placed within the air trenches. Blue arrows represent the displacement current. The magnetic response of the meta-resonator is described in Supplementary Note 2 and highlighted in Supplementary Fig. 3. **d** Normalized dielectric displacement spectral response at the capacitance and inductance.

Solution of Laplace homogeneous equation using an “ideal” metatronic analog processor.

For validating the functionality of the prototyped nano-optic circuit as constituent node of the proposed nanocircuit mesh, we find the solution of a steady-state heat transfer problem in a uniform domain. For demonstration purposes only, we consider the diffusion problem Eq. 1 with Dirichlet boundary conditions, setting the temperature T at the left edge of a rectangular domain L , with H and W height and width of the domain, respectively (Fig. 4a, further details on the derivation provided in the SI). The resistive circuit that solves the finite difference method of a 3×3 mesh is shown in Fig. 4b, it can be numerically solved using a “spice tool”, thus obtaining current and voltage distribution. The boundary conditions that mimic the fixed temperature “potential” at the boundary is a voltage generator V , while the heat sink is a simple connection to the ground (relative GND or simply unbiased). The thermal conductivity k of the medium is modeled in the electrical circuit assigning the resistors to be defined as $R = L/kA$. Similarly, we numerically simulate, by using commercially available full-wave simulation software (further details in Methods section of the SI), the electric field displacement and the displacement current in a 3×3 metatronic mesh. A snapshot of the simulation result of the distribution of the electric field in the middle plane is depicted in

Fig. 4c. Here, a strong local electric field, generated by a horizontal dipole, is used to model the heat source, while the ENZ condition is applied to the remainder of the boundaries. In this section, as an illustrative and not limiting example, the permittivity of the circuit board is considered to have negligible losses⁴¹ $\epsilon'' \approx 0$ with an overall size d of 1000 nm, smaller than the operational wavelength (i.e., $d < \lambda$) to ensure coupling between the nanoelements, as required for conventional electronic circuit concepts at low frequencies^{16,42}. However, the “spatially static-like” properties of the ENZ substrate, i.e., absence of a significant phase variation in ENZ (Supplementary Fig. 1 and Supplementary Movie 1), essentially relaxes this requirement for the optical nano-circuit board of Fig. 4c, for which the total length may become also several free-space wavelengths long (while it is electrically small compared to the very long wavelength in ENZ)¹⁶. Additional details are provided in Supplementary Note 1.

Under these conditions, the field lines in Fig. 4c highlight that the electric displacement, and consequently the displacement current, fall only within the air grooves, forced by the ENZ conditions in the neighboring area ($D \approx 0$). Solution of the PDE problem from different mesh densities in a circuit with ENZ material with negligible losses ($\epsilon \approx 0$) suggests mesh scalability (Fig. 4d). Interestingly, solutions of the PDE adopting a

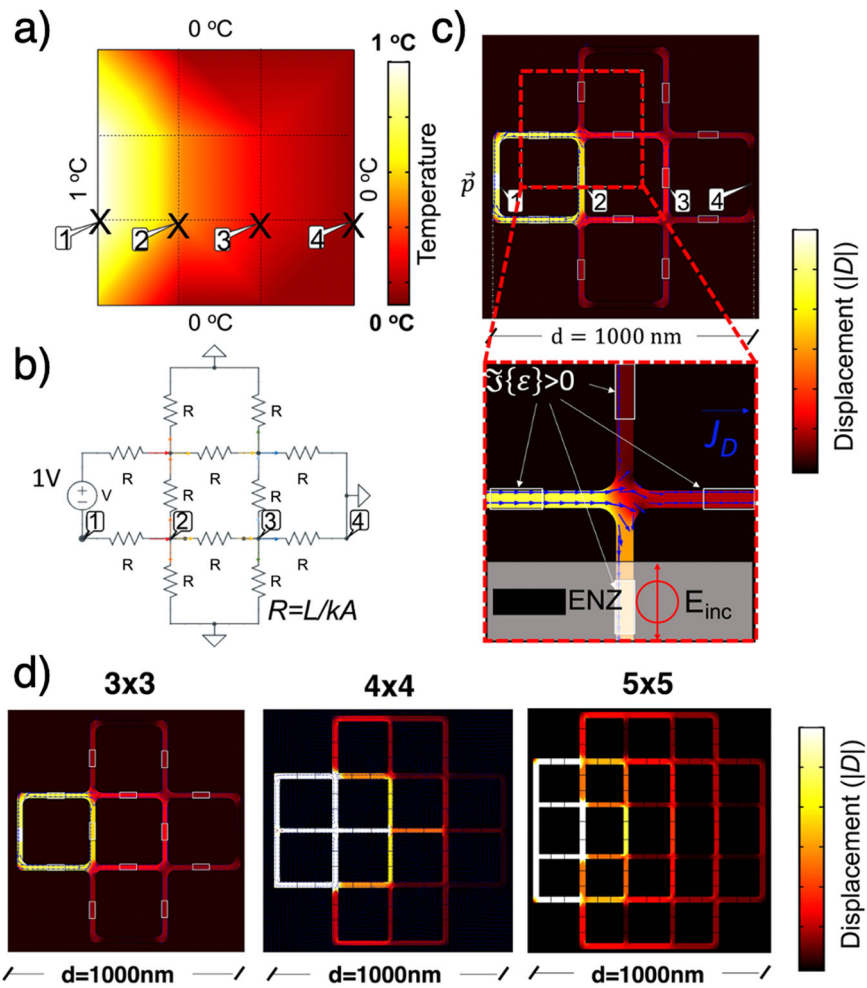


Fig. 4 Heat transfer solution using a metatronic circuit. **a** Mesh equivalence between finite difference, **b** resistive mesh, and **c** metatronics. Zoom in correspondence of the node, showing the displacement current (blue arrows) following the current path scheme of an electrical mesh. No dielectric displacement current is present in the loss-less epsilon-near-zero (ENZ) board. **d** Normalized displacement field as a function of the mesh density (3×3 , 4×4 , 5×5) highlights enhanced accuracy analogously to increased resolution in finite differences method (Supplementary Fig. 4). Leakage from the top surface of the structure is present, but not elevated as shown in Supplementary Fig. 5 and described in Supplementary Note 4.

metatronic processor with increasing mesh density keeping the overall circuit dimension maps precisely the solution of a finer mesh in a finite difference approach, provided the circuit board is characterized by negligible losses, i.e., absence of a dielectric displacement field in the ENZ circuit board, providing a perfect lumped-element electric-circuit behavior. However, a study of the size and scalability and their impact on the accuracy of the solution of the metatronic processor becomes determinant if the losses in the ENZ circuit board, or the deviation from the ideal zero permittivity condition, are not negligible. Other parameters, such as width of the waveguide and smoothness of the bending curves, analyzed in Supplementary Fig. 2a, can affect the accuracy of the solution, and will be discussed elsewhere, and systematic errors could be compensated or mitigated by accurate and controlled processes.

Fixing the mesh density of the simulations, the discretized solutions provided by finite differences method (temperature) and the electromagnetic simulation at the node (local electric field displacement) are normalized to their maximum value and compared. The PDE solution shown by this nanophotonic engine is in high qualitative and quantitative agreement (>95%) with respect to solution obtained using commercial software. Further details between the analytic solution of the Laplace equation, the discretized solution obtained through numerical simulations

(FDM), and the normalized dielectric displacement at each node for different mesh densities is described in Supplementary Note 3.

Other kind of elliptic PDE can also be solved using a different circuit configuration as described in Supplementary Note 7 where a non-homogeneous, second-order, elliptic PDE is solved using a finite difference approach mapped onto a metatronic circuit.

Monolithic integration of reprogrammable metatronic processor for approximate computing.

Recently, a few materials have been considered for fabricating a metatronic circuit board, such as multilayered stacks of thin film⁴³, NP assemblies, and graphene⁴⁴. However, their large-scale integration is far from easy. Here we utilize ITO as a suitable material for a monolithic integration of the proposed metatronic processor (Fig. 5a), which enables distinctive functionalities and is being regularly processed by the consumer electronics such as the touchscreen of every tablet and smart phone, for example. The advantages of using ITO are manifold: (1) ITO has a tunable and controllable optical and electrical properties in the NIR according to process parameters (e.g., oxygen and argon flow rate while sputtering, temperature and environment conditions in thermal annealing processes); (2) as previously demonstrated, its optical properties, imaginary and real part of the permittivity, can be electrostatically

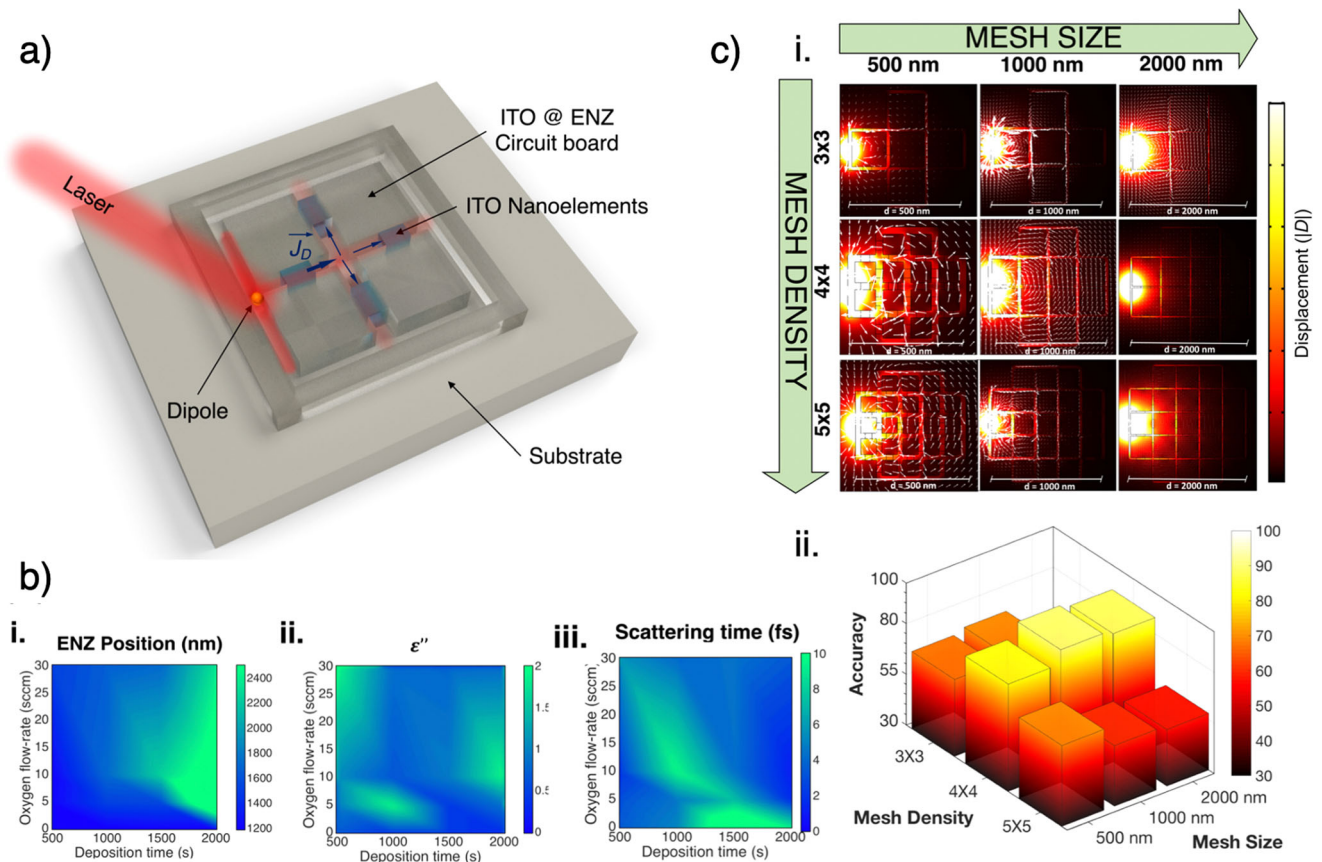


Fig. 5 Monolithic integration of a metatronic circuit board solely based on indium tin oxide. **a** Conceptual sketch of a node of a metatronic circuit based on indium tin oxide (ITO) at epsilon-near-zero (ENZ). A directional antenna is used for coupling the electromagnetic radiation within the trenches, partially filled with dissipative nanoelements which model resistances. A metallic tip of a scanning near-field optical microscope is used for collecting the local near-field displacement and reconstruct the decay. **b** (i-iii) Experimental results obtained through spectroscopic ellipsometry. ENZ wavelength (i), corresponding losses and scattering time τ_{sc} (ii) as a function of process parameters (oxygen flow rate and deposition time). **c** (i) Electric field displacement (heat map) in an ITO metatronic processor as function of mesh size (columns) and mesh density (rows). Displacement current is represented as white arrows. (ii) Solution accuracy as a function of the mesh density and size, compared to a commercially available solver as a function of mesh density and size.

tuned^{35,36,45}, by carrier injection, thus allowing potentially GHz-fast energy-efficient^{22,46} reprogrammability features on the circuit board; and (3) ITO has high manufacturability potential (Supplementary Figs. 6 and 7). Moreover, recently, our group achieved a consistent control over ITO optical parameters with respect to the ENZ wavelength as a function of sputtering parameter, thus allowing to bridge the technological gap in the implementation of metatronic circuits²¹. According to our experimental studies (additional information on film characterization provided in Supplementary Note 5) depicted in Fig. 5b, the ITO for the ENZ circuit board could potentially be sputtered with 5 standard cubic centimeters per minute (sccm) oxygen flow rate, enabling a 200 nm film in ENZ condition at 1550 nm, with non-negligible losses $\tilde{\epsilon} = 0.3i$ which corresponds to a scattering time $\tau = 0.2$ fs. The resistors can be deposited using 20 sccm oxygen flow rate, which yields to $\tilde{\epsilon} = 1.2 + 0.6i$ and a scattering time of 5 fs. The main limitations of the ITO metatronic processor are the unwanted losses in the ENZ circuit board.

Because of the losses in the ITO circuit board, the lines of the displacement field are not fully contained in the air grooves, contrarily to the case of an ENZ material with negligible losses, deviating its behavior from a purely lumped-element circuit. This translates into an inaccurate solution which turns to a faster spatial decay compared to the analytical solution. This deviation is highlighted in Supplementary Fig. 3.

In the presence of non-negligible losses in the ENZ material, the circuit board is not completely insulating, since the displacement current is not negligible:

$$J_D = \frac{\partial D}{\partial t} = \epsilon'' \omega E(\omega) \quad (7)$$

There are two major coexisting phenomena that impact the accuracy of the PDE solution, both of which depend on the ITO losses (Fig. 5c): the first one is a function of the mesh density and the second one of the total physical length of the circuit board. High density ($>5 \times 5$) induces coupling within wires that should not be connected, while the larger physical length ($>2 \mu\text{m}$) contributes to unwanted dissipation, deviating from the original solution. The accuracy as a function of the number of nodes and physical dimension of the circuit board is given in Fig. 5c. The maximum accuracy ($>90\%$) is obtained for a $1 \mu\text{m}$ size mesh, with a 4×4 mesh density. This is achieved thanks to the trade-off between mesh size and density, which minimizes the wire coupling, without extending the wiring length, producing unwanted losses.

As previously discussed, the ITO layer can be in a capacitor configuration, spaced by a thin dielectric, for electrostatic doping, enabling fine-tuning of the permittivity values (Fig. 5b) as well as reprogramming the circuit for mapping different problems. The variation of the carrier density via gating in ITO affects both resistance and reactance in the metatronics equivalent circuit,

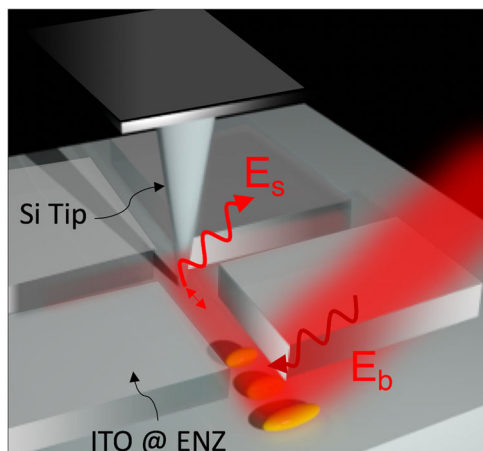


Fig. 6 Schematic representation of a possible experimental demonstration of a reconfigurable nano-optical circuit board and solver.

Impinging radiation (E_b) excites a directional antenna, which generates a local near-field. The local near-field produces a dielectric displacement within a metatronic circuit made of indium tin oxide (ITO) operating at its epsilon-near-zero (ENZ). The displacement can be probed by measuring the scattered near-field (E_s) produced by the metal tip of a scattering-type scanning near-field optical microscope (s-SNOM) or by a nanophotonic probe card (NPC) (Supplementary Fig. 8a), which consists of an array of several apertures (numerical simulations are presented in Supplementary Fig. 8b).

hindering the accuracy of the solution, being imaginary, and the real part of the permittivity. Nevertheless, contrary to the resistive circuit, if either the boundary conditions or the impedances are rapidly “programmed”, the nano-optic equivalent circuit is not affected by dispersion. This is possible because, unlike electric circuit, here the modulation speed can be RC-element large, which is independent from the overall circuit (unlike an electronic circuit). The signal modulation timescales ($<ns$) are much larger than the propagation delay of the electromagnetic waves across the lumped element. In this case, in fact, the lumped circuit model would hold, since even at 100 s of GHz, the timescale at which the carrier signal is modulated does so substantially slower than the time taken by the optical signal to travel through the nano-optics network.

Additionally, besides affecting the accuracy of the solution, the losses affect the power consumption and dissipation. For a processor with a contained size, an approximate solution is always guaranteed. The power consumption from the processor is the summation of the optical power used for exciting the dipole (initiating the processor) and the radio frequency power employed for modulating the carrier density of each lumped elements, i.e., reprogramming the circuit. Concerning the reconfigurability of the processor, recent works showed few femtojoule-efficient ITO-based modulators, potentially operating at high-speed^{22,46} (see Supplementary Fig. 7 for GHz-fast experimental ITO modulation). On the other hand, a few milliwatts of optical power is needed for exciting the fluorescent molecule and setting the boundary conditions. Efficient measurement schemes must be used to detect the electric field displacement at each node of the metatronic mesh, avoiding scanning over the sample, e.g., high-resolution tip-enhanced near-field spectroscopy, to minimize the power used for the detection mechanism.

As a final remark, the constraint on the engine footprint given by the effective wavelength at ENZ and the minimum internode distance, for avoiding unwanted coupling of neighboring wires in a lossy ENZ material, hinders the implementation of high

number of nodes. A possible solution would be trading off reconfigurability and using non-reprogrammable near-zero materials characterized by negligible losses or photonic wires³². Other challenges of a possible implementation are discussed in Supplementary Notes 8 and 9.

Discretized solutions with nano-optic probe card. In order to sample the electric field displacement signal at the nodes of the metatronic mesh, deep sub-wavelength near-field microscopy must be employed with nanometric spatial resolution, which can be used for investigating the local near-field, breaking the diffraction limit. (Fig. 6) A s-SNOM in transmission, which uses a dielectric tip can be employed for measuring the dielectric displacement, in a similar configuration shown in⁴⁷ with a resolution of a few nanometers in the lateral dimension. The s-SNOM would scan the entire ENZ board and its trenches in tapping mode. The radiation is conveyed from the bottom using a focused light which by impinging on a QD, excites a strong near-field within the trenches. Further details on launching propagating mode using optical antenna or dipole at mesh node are discussed in Supplementary Notes 6 and 9. The scattered radiation from the tip is collected by a parabolic mirror and provides information of the complex optical properties of the nanoscale region in proximity of the tip. By using the s-SNOM, it is possible to retrieve both amplitude and phase of the background-free local electric near-field. However, regular near-field optical microscopes, such as scattering-type near field, are associated with AFM systems, thus requiring long scanning time. For this purpose, a nanophotonic probe card could potentially read the values of the local displacement field (see Supplementary Fig. 8), similarly to a wafer probe for electrical testing. The reading mechanism is based on an array of dielectric tips characterized by a sub-wavelength aperture at the apex⁴⁸, which collects the local near-field radiation similarly to a local near-field microscope, allowing for parallel readout. Aperture SNOM would be preferential with respect to scattering type (s-SNOM), since the former will minimize the coupling between vertical dipoles, i.e., metallic tip, while the latter can introduce second-order scattering and a higher degree of uncertainty in the system.

In conclusion, here we introduced a nano-optic metatronic-based integrated engine, operating in the optical telecommunication band, based on a sub-wavelength epsilon-near zero (ENZ) circuitry. We mathematically prove that the mesh current method of a metatronic circuit, which mimics a lumped-element electrical circuit, can map a finite difference mesh that solves a steady-state Laplacian equation and, by extension, other time-variant second-order elliptic PDEs. Moreover, in contrast with a resistive network, we numerically show that this technology can be used to solve PDEs with high accuracy (90%), while decoupling circuit mesh upscaling from reprogramming speed. Beyond a theoretical framework, we showed through numerical simulation that this metatronic circuit solver can be realized using one single material, exploiting the ability to tailor the optical properties of ITO, sputtered using, experimentally validated, controlled process parameters, thus enabling a high degree of manufacturability. This analog processor is particularly well-suited to be reprogrammed on both the boundary conditions and network elements, limited in size only by the presence of ohmic losses. Implementing these techniques enables an ultrafast, chip-scale, integrable, and reconfigurable analog computing processor that is able to solve PDEs at the speed of light without lumped circuit capacitance delay.

Methods

The numerical simulations of this study were carried out using commercially available software Comsol Multiphysics, we used the frequency-dependent solver

with a tetrahedron mesh. The dimension of the maximum meshing element of the metatronic board was $1/100$ of λ and a denser local mesh was considered for the air grooves and the lumped components. The electric field was excited by a point dipole moment of amplitude 1 V. The ITO film's optical properties (complex permittivity and thickness) and relative sputtering process parameters (oxygen/argon flow rate, deposition time, annealing time and temperature) were taken from Silva et al.¹⁸. The effects of the carrier injection to the dispersion of the ITO film in the near-infrared region was derived using Drude's model. Complex refractive index, scattering rate, ENZ wavelength, initial carrier concentration, thickness, and plasma frequency were derived by spectroscopic ellipsometry of the deposited film and used as fitting parameters for the active tuning. Further details regarding the methods used in this study can be found in Supplementary Note 5.

Data availability

All data needed to evaluate the conclusions in the paper are present in the paper or the Supplementary Online Materials. Additional data available from authors upon request.

Received: 15 September 2020; Accepted: 21 July 2021;

Published online: 26 August 2021

References

1. Tsividis, Y. Not your Father's analog computer. *IEEE Spectrum* **55**, 38–43 (2018).
2. Ambrogio, S. et al. Equivalent-accuracy accelerated neural-network training using analogue memory. *Nature* **558**, 60 (2018).
3. Zidan, M. A. et al. A general memristor-based partial differential equation solver. *Nat. Electron.* **1**, 411–420 (2018).
4. Shen, Y. et al. Deep learning with coherent nanophotonic circuits. *Nat. Photonics* **11**, 441–446 (2017).
5. Miscuglio, M. et al. All-optical nonlinear activation function for photonic neural networks [Invited]. *Opt. Mater. Express, OME* **8**, 3851–3863 (2018).
6. Rios, C. et al. In-memory computing on a photonic platform. *Sci. Adv.* **5**, eaau5759 (2019).
7. Miscuglio, M. & Sorger, V. J. Photonic tensor cores for machine learning. *Appl. Phys. Rev.* **7**, 031404 (2020).
8. Lin, X. et al. All-optical machine learning using diffractive deep neural networks. *Science* **361**, 1004–1008 (2018).
9. Mohammadi Estakhri, N., Edwards, B. & Engheta, N. Inverse-designed metamaterials that solve equations. *Science* **363**, 1333–1338 (2019).
10. Heuck, M., Jacobs, K. & Englund, D. R. Controlled-phase gate using dynamically coupled cavities and optical nonlinearities. *Phys. Rev. Lett.* **124**, 160501 (2020).
11. Liebmann, G. Solution of partial differential equations with a resistance network analogue. *Br. J. Appl. Phys.* **1**, 92–103 (1950).
12. Rocca, E. & Rossi, R. 'Entropic' solutions to a thermodynamically consistent PDE system for phase transitions and damage. *SIAM J. Math. Anal.* **47**, 2519–2586 (2015).
13. Borggaard, J. & Burns, J. A PDE sensitivity equation method for optimal aerodynamic design. *J. Comput. Phys.* **136**, 366–384 (1997).
14. Crank, J. & Nicolson, P. A practical method for numerical evaluation of solutions of partial differential equations of the heat-conduction type. *Adv. Comput. Math.* **6**, 207–226 (1996).
15. Cheshire, G. & Henshaw, W. D. Composite overlapping meshes for the solution of partial differential equations. *J. Comput. Phys.* **90**, 1–64 (1990).
16. Li, Y. et al. On-chip zero-index metamaterials. *Nat. Photonics* **9**, 738–742 (2015).
17. Caglayan, H., Hong, S.-H., Edwards, B., Kagan, C. R. & Engheta, N. Near-infrared metatronic nanocircuits by design. *Phys. Rev. Lett.* **111**, 073904 (2013).
18. Silva, A. et al. Performing mathematical operations with metamaterials. *Science* **343**, 160–163 (2014).
19. Lumer, Y., Liberal, I. & Engheta, N. Quantum features of optical metatronics. In *2017 Conference on Lasers and Electro-Optics (CLEO)* 1–2 (OSA, 2017).
20. Lumer, Y. & Engheta, N. Circuit modularization of quantum optical systems. *Phys. Rev. Appl.* **14**, 054034 (2020).
21. Gui, Y. et al. Towards integrated metatronics: a holistic approach on precise optical and electrical properties of indium tin oxide. *Sci. Rep.* **9**, 11279 (2019).
22. Amin, R. et al. Sub-wavelength GHz-fast broadband ITO Mach-Zehnder modulator on silicon photonics. *Optica* **7**, 333–335 (2020).
23. Chaudhari, P., Oberman, A., Osher, S., Soatto, S. & Carlier, G. Deep relaxation: partial differential equations for optimizing deep neural networks. *Res. Math. Sci.* **5**, 30 (2018).
24. Perona, P. & Malik, J. Scale-space and edge detection using anisotropic diffusion. *IEEE Trans. Pattern Anal. Mach. Intell.* **12**, 629–639 (1990).
25. Aletti, G., Moroni, M. & Naldi, G. A new nonlocal nonlinear diffusion equation for data analysis. *Acta Appl. Math.* **168**, 109–135 (2020).
26. Palmer, P. J. *Investigations Into the Use of an Electrical Resistance Analogue for the Solution of Certain Oscillatory-flow Problems* (H.M. Stationery Office, 1957).
27. Liebmann, G. Resistance-network analogues with unequal meshes or subdivided meshes. *Br. J. Appl. Phys.* **5**, 362–366 (1954).
28. Edwards, B. & Engheta, N. Experimental verification of displacement-current conduits in metamaterials-inspired optical circuitry. *Phys. Rev. Lett.* **108**, 193902 (2012).
29. Liu, N. et al. Individual nanoantennas loaded with three-dimensional optical nanocircuits. *Nano Lett.* **13**, 142–147 (2013).
30. Shi, J. et al. Modular assembly of optical nanocircuits. *Nat. Commun.* **5**, 1–8 (2014).
31. Alù, A. & Engheta, N. All optical metamaterial circuit board at the nanoscale. *Phys. Rev. Lett.* **103**, 143902 (2009).
32. Liu, R., Roberts, C. M., Zhong, Y., Podolskiy, V. A. & Wasserman, D. Epsilon-near-zero photonics wires. *ACS Photon.* **3**, 1045–1052 (2016).
33. Liberal, I., Mahmoud, A. M., Li, Y., Edwards, B. & Engheta, N. Photonic doping of epsilon-near-zero media. *Science* **355**, 1058–1062 (2017).
34. Boltasseva, A. & Atwater, H. A. Low-loss plasmonic metamaterials. *Science* **331**, 290–291 (2011).
35. Lee, H. W. et al. Nanoscale conducting oxide PlasMOSstor. *Nano Lett.* **14**, 6463–6468 (2014).
36. Sorger, V. J., Lanzillotti-Kimura, N. D., Ma, R.-M. & Zhang, X. Ultra-compact silicon nanophotonic modulator with broadband response. *Nanophotonics* **1**, 17–22 (2012).
37. Lu, H., Carroll, G. M., Neale, N. R. & Beard, M. C. Infrared quantum dots: progress, challenges, and opportunities. *ACS Nano* **13**, 939–953 (2019).
38. Zhang, Y. et al. Broadband transparent optical phase change materials for high-performance nonvolatile photonics. *Nat. Commun.* **10**, 1–9 (2019).
39. Feigenbaum, E., Diest, K. & Atwater, H. A. Unity-order index change in transparent conducting oxides at visible frequencies. *Nano Lett.* **10**, 2111–2116 (2010).
40. Li, E., Gao, Q., Chen, R. T. & Wang, A. X. Ultracompact silicon-conductive oxide nanocavity modulator with 0.02 lambda-cubic active volume. *Nano Lett.* **18**, 1075–1081 (2018).
41. Silveirinha, M. G., Alù, A., Li, J. & Engheta, N. Nanoinsulators and nanocircuits for optical nanocircuits. *J. Appl. Phys.* **103**, 064305 (2008).
42. Moitra, P., Slovick, B. A., Gang Yu, Z., Krishnamurthy, S. & Valentine, J. Experimental demonstration of a broadband all-dielectric metamaterial perfect reflector. *Appl. Phys. Lett.* **104**, 171102 (2014).
43. Li, Y., Liberal, I., Della Giovampaola, C. & Engheta, N. Waveguide metatronics: lumped circuitry based on structural dispersion. *Sci. Adv.* **2**, e1501790 (2016).
44. Vakil, A. & Engheta, N. Transformation optics using graphene. *Science* **332**, 1291–1294 (2011).
45. Tahersima, M. H. et al. Coupling-enhanced dual ITO layer electro-absorption modulator in silicon photonics. *Nanophotonics* **8**, 1559–1566 (2019).
46. Li, E., Nia, B. A., Zhou, B. & Wang, A. X. Transparent conductive oxide-gated silicon microring with extreme resonance wavelength tunability. *Photon. Res.* **7**, 473–477 (2019).
47. Alonso-González, P. et al. Controlling graphene plasmons with resonant metal antennas and spatial conductivity patterns. *Science* **344**, 1369–1373 (2014).
48. Bao, W. et al. Mapping local charge recombination heterogeneity by multidimensional nanospectroscopic imaging. *Science* **338**, 1317–1321 (2012).

Acknowledgements

This work was supported by National Science Foundation (1748294) grant.

Author contributions

V.J.S. and T.E.G. envisioned the idea of a reprogrammable optical computer, acquired the funds, and supervised the project. M.M. and V.J.S. conceived the nano-optic platform for analog computing. M.M. developed the relevant theories and analyses for the project, and designed the nano-optic circuit. Y.G. and M.M. conducted the spectroscopy ellipsometry experiments. Z.M., S.S., and X.M. conducted numerical simulations. M.M., A.A., and V.J.S. discussed the results and contributed to the understanding, analysis, and interpretation of the results. M.M. wrote the first draft of the manuscript. V.J.S., A.A., T.I., and T.E.G. contributed to writing subsequent drafts of the manuscript.

Competing interests

The authors have filed a provisional patent application on this idea, U.S. Patent 10,318,680. No other conflict of interest is present.

Additional information

Supplementary information The online version contains supplementary material available at <https://doi.org/10.1038/s42005-021-00683-4>.

Correspondence and requests for materials should be addressed to M.M. or V.J.S.

Peer review information *Communications Physics* thanks the anonymous reviewers for their contribution to the peer review of this work.

Reprints and permission information is available at <http://www.nature.com/reprints>

Publisher's note Springer Nature remains neutral with regard to jurisdictional claims in published maps and institutional affiliations.



Open Access This article is licensed under a Creative Commons Attribution 4.0 International License, which permits use, sharing, adaptation, distribution and reproduction in any medium or format, as long as you give appropriate credit to the original author(s) and the source, provide a link to the Creative Commons license, and indicate if changes were made. The images or other third party material in this article are included in the article's Creative Commons license, unless indicated otherwise in a credit line to the material. If material is not included in the article's Creative Commons license and your intended use is not permitted by statutory regulation or exceeds the permitted use, you will need to obtain permission directly from the copyright holder. To view a copy of this license, visit <http://creativecommons.org/licenses/by/4.0/>.

© The Author(s) 2021